Jean-Paul Martin[1]
Bio-Mechatronics and Robotics Laboratory,
Department of Mechanical and
Materials Engineering,
Queen's University,
Kingston, ON K7L 3N6, Canada

Michael Shepertycky[1]
Bio-Mechatronics and Robotics Laboratory,
Department of Mechanical and
Materials Engineering,
Queen's University,
Kingston, ON K7L 3N6, Canada

Yan-Fei Liu
Power Group,
Department of Electrical and
Computer Engineering,
Queen's University,
Kingston, ON K7L 3N6, Canada

Qingguo Li
Bio-Mechatronics and Robotics Laboratory,
Department of Mechanical and
Materials Engineering,
Queen's University,
Kingston, ON K7L 3N6, Canada

Lower Limb-Driven Energy Harvester: Modeling, Design, and Performance Evaluation

Biomechanical energy harvesters (BMEHs) have shown that useable amounts of electricity can be generated from daily movement. Where access to an electrical power grid is limited, BMEHs are a viable alternative to accommodate energy requirements for portable electronics. In this paper, we present the detailed design and dynamic model of a lower limb-driven energy harvester that predicts the device output and the load on the user. Comparing with existing harvester models, the novelty of the proposed model is that it incorporates the energy required for useful electricity generation, stored inertial energy, and both mechanical and electrical losses within the device. The model is validated with the lower limb-driven energy harvester in 12 unique configurations with a combination of four different motor and three different electrical resistance combinations (3.5 Ω, 7 Ω, and 12 Ω). A case study shows that the device can generate between 3.6 and 15.5 W with an efficiency between 39.8% and 72.5%. The model was able to predict the harvester output peak voltage within 5.6 ± 3.2% error and the peak force it exerts on the user within 9.9 ± 3.4% error over a range of parameter values. The model will help to identify configurations to achieve a high harvester efficiency and provide a better understanding of how parameters affect both the timing and magnitude of the load felt by the user. [DOI: 10.1115/1.4033014]

1 Introduction

With the advancement of portable electronics such as cell phones and laptops, we have come to rely on frequent access to electricity sources for charging our devices. But for those who depend on life saving electronics to survive, a different relationship with electricity begins to exist, one beyond convenience; field scientists, explorers, disaster-relief workers, or those using powered medical devices depend on electricity to power their communication, global positioning systems, scientific equipment, or medical devices. Currently, these portable electronics are almost exclusively powered by batteries, often rechargeable. Batteries themselves, however, are limited by the amount of energy they can store per unit mass [1]. Two solutions present themselves to satisfy electricity requirements when access to a power source is not an option. First, the user can choose to carry the weight of extra batteries needed to support all devices for the entire trip duration. When considering energetically demanding devices, or perhaps multiple devices and over an extended duration, the weight in batteries required becomes impractical for the user to bear. As a second alternative, renewable energy sources have shown to be a viable solution to satisfy the energy requirements for devices off-the-grid [2–5].

BMEHs, generating electricity during daily activities, operate on the premise that food has more energy per unit mass than batteries and are therefore a more energy dense storage facility [6]. Researchers have developed various ways to harvest electricity from human motion [1,2]. These devices are typically categorized by the principle in which they harvest electricity from the user. Inertial-based harvesters generate electricity from the inertial force of a proof mass [7–13], such as a load suspended on a backpack frame capable of generating 7.4 W [8] with a device weight of 5.6 kg. Impact force-based harvesters use external forces to generate electricity [14–17]. Popular devices have targeted the impact force during heel strike, where one, by magnifying the vertical sole deformation of a shoe using trapezoidal sliders and a gear train, was able to produce 1 W of electricity [17]. Finally, movement-driven harvesters use the motion of limb segments moving relative to one another to drive electromagnetic generators [18–22]. Donelan et al. developed an energy harvester by altering an orthopedic brace to harvest negative work of the knee joint during the end of swing phase of walking, producing up to 5 W of electricity with a pair of devices weighing a total 3.3 kg [23]. Instead of continuously generating electricity, their device selectively targeted negative work regions, assisting musculature in dissipating energy in the negative work phase. Similarly, Shepertycky and Li targeted lower-limb motion during negative work regions of swing phase [20]. By doing so, the lower-limb harvester was able to generate 9 W (2.5 Ω resistance) of electricity by harvesting motion from both limbs at a total system weight of 2.66 kg (device: 0.95 kg, backpack: 1.19 kg, rectifying circuit: 0.39 kg, and shoe harnesses: 0.13 kg). Of the mentioned devices, only four [8,13,20,23] have shown to be able to generate substantial amounts of electrical power (>5 W) suitable for more demanding portable electronics such as laptops (∼25 W), mobile phones (∼1 W), or powered prosthetics (∼1 W) [24–26].

Of the aforementioned high-power BMEH devices, device–user interaction is typically experimentally quantified by measuring alterations in gait patterns and measuring user effort [8,20,23]. However, experimentally determined effects allow for limited interrogation of the device–user interaction. They only show the end effect on the user and give no insight into what device behavior may cause changes in user effort. As the goal of a BMEH is to generate more electricity while simultaneously reduce user effort, by considering parameter relationships through modeling, we aim to decrease BMEH's electrical and mechanical losses, decrease device weight, and control how we transfer load to the user such that it has the smallest effect on the user's gait pattern and effort.

[1]J.-P. Martin and M. Shepertycky contributed equally to this work.

Manuscript received June 4, 2015; final manuscript received February 5, 2016; published online August 24, 2016. Assoc. Editor: Carl Nelson.

In this paper, we aim to complement the knowledge gained from Ref. [20], where the lower limb-driven energy harvester was first introduced with a focus on understanding the energetic consequences of the harvester usage through human experimentation. It was shown that the harvester could generate electricity efficiently with a minimal impact on the user's gait when the electrical load is small. In this paper, we present the in-depth description of the harvester design to achieve a better understanding of device function. Most importantly, a dynamic BMEH model, expanding off the work of Shepertycky [27], is developed to determine the load applied to the user by the device and the harvester electrical power output. We propose this as an alternative to the equivalent electrical component model developed by Rubinshtein et al. [21].

For a given harvester topology, there are many design parameters that could affect the harvester performance (e.g., amount of power production and the user power input). Li et al. [6] proposed a quasi-static model for the knee-mounted harvester and were able to predict the power and torque for a given input motion profile. Xie and Cai [17] similarly modeled their heel strike device quasi-statically to predict output electrical power. However, these models only predict the load on the user due to the electrical power generation. Their models neglect the inertial force required for accelerating the device's components and the device friction, which might consequently underestimate the total load applied to the user. This is especially true in the case of high device acceleration. In addition, only Xie and Cai provided data from human experimentations to validate the accuracy of the proposed model [17]. Here, we present a new dynamic model of the harvester, which overcomes limitations of previous harvester models and provides a connection between controllable device parameters and changes in user loading. The proposed model approximates performance measures of the harvester based on an input kinematic profile and known harvester parameters. The first performance measure is the output voltage from which output electrical power can be calculated. The second performance measure is the force the harvester applies to the user, from which the input mechanical power can be calculated. The performance of the proposed model is validated through human experimentation.

2 Lower Limb-Driven Energy Harvester Design

By taking advantage of the unique out-of-phase lower-limb motion during gait, movement of both legs are consolidated into a single power generating unit mounted close to the user's center of mass. A human figure in Fig. 1(*a*) illustrates a user walking with the device over an entire gait cycle. The device harvests electricity when cables, extending from the device and attached to the ankles of the user, are lengthened. Input linear displacement profiles, found as the magnitude of the vectors from the right and left greater trochanter to the right and left heel (Fig. 1(*b*)), show that cable lengthening coinciding with the swing phase of a gait cycle. Linear velocity captured using the device's cables is shown in Fig. 1(*c*), where positive velocity indicates cable lengthening. Regions of positive linear velocity for each leg are out of phase by a half-gait cycle, demonstrating the device's capability in combining the motions of both limbs.

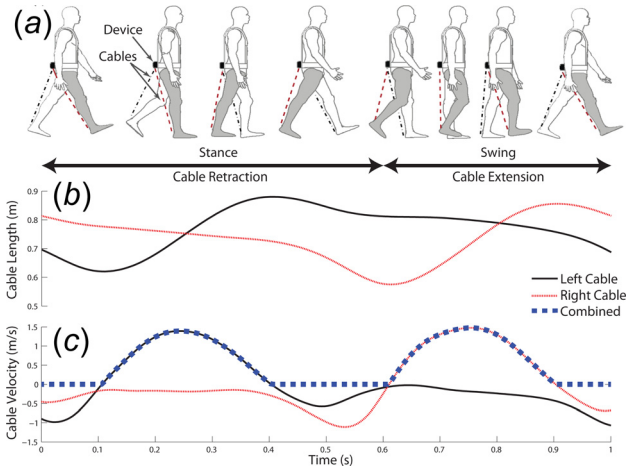

Fig. 1 (*a*) Schematic of a gait cycle indicating time of cable retraction and cable extension of the right leg. (*b*) Both left and right cable length over a complete gait cycle. (*c*) Cable velocity of both left and right cable and combined positive velocity of both cables. Modified from Ref. [20].

The device itself consists of a harvesting unit mounted to the bottom of a backpack frame and a pair of foot harness (Fig. 2(*a*)). Two cables—attached to the foot harnesses—are fed from and retracted into the harvesting unit. Retraction mechanisms within the device coil the excess cable (Fig. 2(*b*)). A gear train amplifies the cable's linear displacement and integrates the motion of each cable into a single rotational motion. The resultant rotation then drives a generator, converting the mechanical energy to electrical energy.

When the cable first enters the device, it passes over an idler pulley, redirecting its path to be coiled around an input pulley. A constant force spring applies a moment about the input pulley to keep the cable taut and retract the cable. Motion is transferred from the input pulley through the input shaft to the drive gear, which is mounted to the input shaft via an one-way roller clutch. The one-way clutch is responsible for engaging the gear train during cable extension and disengaging to allow the cables to retract. Additionally, it disengages when input motion from the opposite limb is driving the gear train. This isolates the input from one limb from affecting the retraction mechanism of the opposite limb.

When the cable is extending, the input shaft and driver gear become coupled, and the angular rotation from the input pulley is transferred to the driven gear through a single stage gear train (gear ratio of 5:1). This converts the high torque, low angular velocity input motion to a low torque, high angular velocity motion more suitable for electric power generation with a miniature generator. The driven gear rotates a generator shaft converting mechanical energy to electrical energy. For model validation purposes, the generated electricity is dissipated in high-power resistors. The electrical load resistor is set by an operator, allowing for control over the mechanical resistance felt by the user and the amount of energy harvested.

3 Harvester Dynamic Model

The design objective for an energy harvester is to generate a substantial amount of electricity (>5 W) while constraining the load on the user such that it exacts a minimal metabolic cost. A dynamic model will help to understand how a network of interconnected device parameters can be determined to achieve optimal device performance. The model uses the input profile representative of the motion inputted into the harvester system by the user. For the lower limb-driven energy harvester, the input kinematic profile is Fig. 1(*c*).

The lower limb-driven harvester operates in two states: coupled, where cable lengthening causes generator shaft rotation, and decoupled, where the one-way clutch disengages the input shaft from the generator shaft. Similarly, these states exist for other harvester types—either the user is actively inputting energy in to the system or the system remains passive. During a coupled state, the force exerted on the user is proportional to both resistances from electrical generation and from passive mechanical elements of the entire system. Conversely, in a decoupled state, only passive mechanical elements are felt by the user (e.g., retraction mechanism springs). Figures 3(*a*) and 3(*b*) show the engaged components during a coupled and decoupled state, respectively.

There are three scenarios in which decoupling can occur. The first condition is when the input cable is retracting and the one-

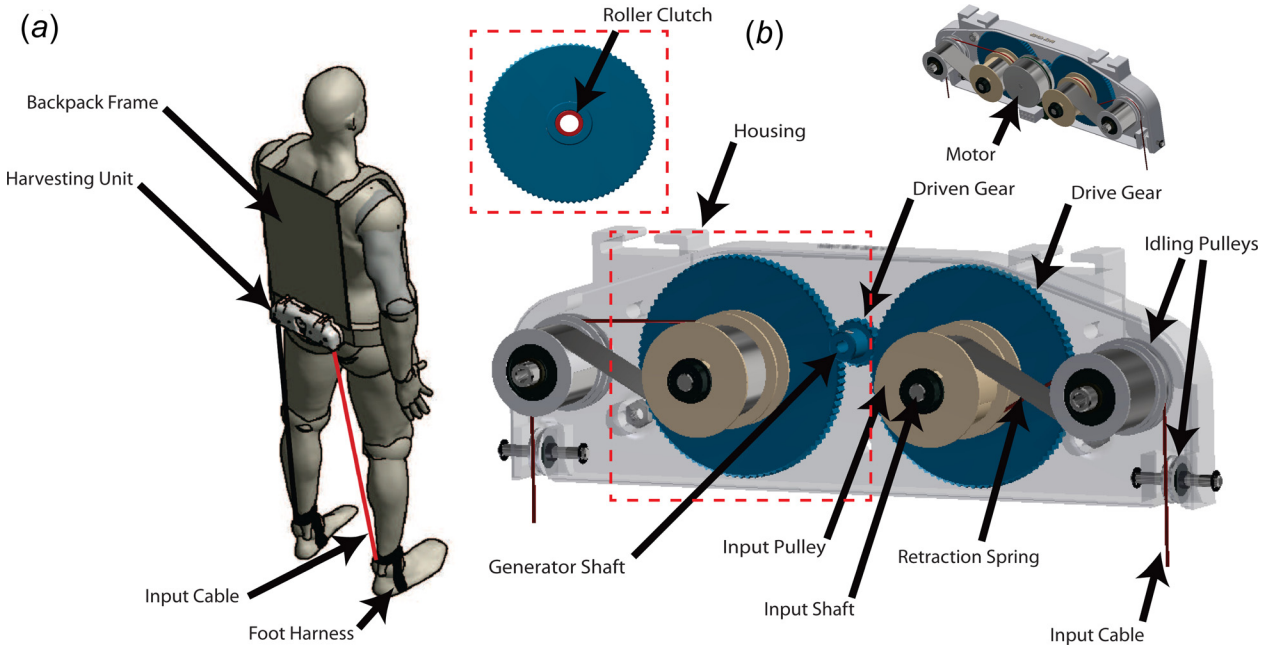

Fig. 2 The lower limb-driven energy harvesting device. (*a*) Schematic showing how the harvester is worn by the user. Modified from Ref. [20]. (*b*) Components of the retraction mechanism: a constant force spring exerting a force on the input pulley, while its other end freely coils about an idler pulley. Cable path: the cable passes over two sets of idler pulleys, redirecting its path to be coiled about the input pulley. Gear train: the input pulley transfers motion to an input shaft. Motion is then transferred to a drive gear via a one-way roller clutch (shown in removed section). The motion is amplified through a single stage gear ratio to the driven gear. The driven gear is mounted on the generator shaft (not shown in the figure).

way clutch does not engage. A second condition is when the opposite limb is driving the gear train faster then the current limb. The last condition, of which has importance to the optimization of device parameters, is when the inertia of the gear train sustains an angular velocity greater than that of the input pulley, causing the drive gear to overrun the input shaft. These phenomena can be observed when comparing the angular velocity of the input shaft and generator shaft (Fig. 4). Figure 4(*b*) shows the angular velocity of the generator shaft, reduced by the gear ratio, overrunning the angular velocity of the input shaft near the end of the input cycle after the time of decoupling, t_c. Figure 4(*a*) shows the components of the gear train during each state. While coupled, the input pulley transfers motion to the drive gear, driven gear (generator shaft), and opposite drive gear. When decoupled, the input pulley rotates independently of the two drive gears and driven gear.

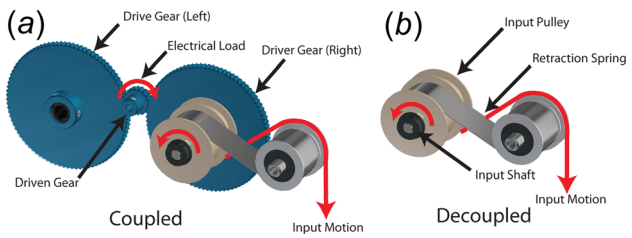

Fig. 3 Schematic showing internal components engaged in each state. (*a*) Coupled state. The input shaft is engaged with the remainder of the system. Engaged components include both left and right drive gears, driven gear, generator, input shaft, input pulley, and the retraction spring. (*b*) Decoupled state. The input shaft is not mechanically engaged with the remainder of the gear train due to the overrun of the roller clutch. Engaged components include input shaft, input pulley, and the retraction spring.

To model the behavior of decoupling, the state is determined at the beginning of each time instant based on the system's kinetics (calculations in Sec. 3.2). A decoupled state is determined by comparing the model's predicted angular velocity at the next time instant to the measured angular velocity at the input. When the system is coupled, the measured input shaft rotational velocity will be used to compute output voltage and cable force. When the system is determined to be in the decoupled state, the model will instead predict the angular velocity of the generator for the next time instant based on the kinetic equations governing the

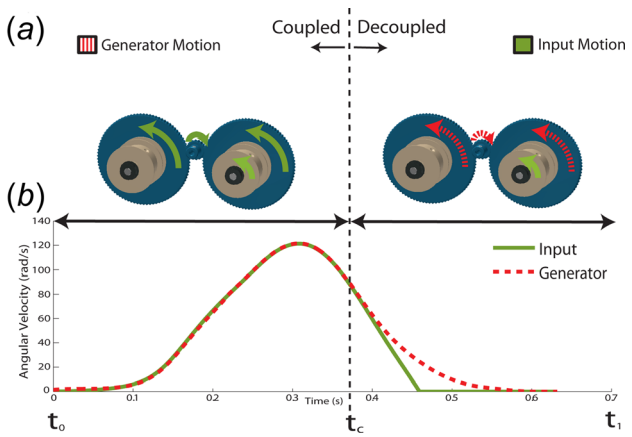

Fig. 4 (*a*) Gear train assembly shows which components of the drive train are rotating at the same speed in each state. (*b*) Input and generator shaft angular velocity as a function of time. The generator shaft angular velocity is reduced by the overall gear ratio for direct comparison. Vertical dashed line indicates the time (t_c) that decoupling begins, where the generator shaft overruns the input shaft. t_0 indicates initiation of swing and t_1 indicates the beginning of swing of the opposite limb.

harvester system. The total harvester reaction force applied to the user is modeled differently for the coupled state and decoupled state in Secs. 3.1 and 3.2.

3.1 Coupled State ($t_o < t < t_c$). In the coupled state, the total harvester reaction torque is divided into three components: torque required to drive the generator, torque required to accelerate device components (device inertia), and the torque to overcome device friction and the gear train inefficiency. Each component's contribution is calculated separately in Secs. 3.1.1–3.1.3.

3.1.1 Generator Reaction Torque. A generator produces a voltage, E_g, dependent on the input velocity to the harvester system

$$E_g = \frac{N \cdot v_i \cdot K_{\text{gr}}}{r_i} \tag{1}$$

where v_i is input cable's linear velocity (Fig. 1(*c*)), amplified by N, the overall gear ratio, and r_i, the radius of the input pulley. K_{gr} is the electromotive force (EMF) constant provided by the generator manufacturer and reported in mV/rad s^{-1}. The EMF constant is dependent on the motor winding's dimensions, turns, and strength of magnetic field [28]. Under the closed circuit condition, the line current i_l can be calculated

$$i_l = \frac{E_g - 2 \cdot E_d}{R_a + R_l + R_r} \tag{2}$$

where R_a is the generator's armature resistance, R_l is the electrical load resistance specified by the user, and R_r is the diode resistance. The AC three-phase voltage generated by the motor is full wave rectified. Since two diodes are always conducting, the forward voltage lost is two times the voltage drop across a single diode, E_d.

When generating electricity, the generator produces a reaction torque, T_{gen}, proportional to the line current, i_l

$$T_{\text{gen}} = i_l \cdot K_t \tag{3}$$

where K_t is the torque constant provided by the motor manufacturer and equates to the EMF constant when expressed in SI units. The generator torque is then applied back to user through the gear train. The gear train amplifies the torque which is then applied to the user through cable tension.

3.1.2 Device Inertia. A second component of the total harvester reaction torque is the torque arising from inertial effects, T_{se}

$$T_{\text{se}} = I_a \cdot \alpha \tag{4}$$

The inertial force is found at a particular location (e.g., the input or the generator), where α is the angular acceleration at that location and I_a is the apparent inertia. The apparent inertia at the input shaft $I_{a,i}$ is found as follows:

$$I_{a,i} = I_{\text{input}} + I_{\text{drive}} + N^2 \cdot I_{\text{generator}} \tag{5}$$

Additionally, $I_{a,g}$ is the apparent inertia at the generator

$$I_{a,g} = I_{\text{generator}} + \left(\frac{1}{N}\right)^2 (I_{\text{drive}} + I_{\text{input}}) \tag{6}$$

where I_{input} is the moment of inertia of the input pulley, shaft, clutch, and drive gear; $I_{\text{generator}}$ is the inertia of the generator and driven gear; and I_{drive} is the inertia of the drive gear and clutch. The angular acceleration at the generator shaft is simply the angular acceleration at the input shaft recorded from the encoder amplified through the gear train.

3.1.3 Friction Torque. The last component of the total harvester reaction torque is the torque required to overcome device friction. We assumed that the mechanical friction of the system is a sum of both bearing and gear train friction for modeling purposes. The frictional moment due to a bearing, T_b, is found as follows [29–31]:

$$T_b = 0.5 \cdot \mu \cdot d \cdot \left(\frac{T}{R} \cdot \tan(\theta_{\text{pitch}}) + F\right) \tag{7}$$

where μ is the coefficient of friction specified by the manufacturer, d is the bearing bore diameter for deep groove ball bearings or diameter under rollers for needle bearings, T is the torque being applied to the gear, R is the radius of the gear, θ_{pitch} is the pitch angle of the gear, and F is the sum of radially directed loads on the shaft.

Additionally, the load transferred through the gear train is subject to the gear train efficiency

$$T_{\text{out}} = T_{\text{in}} \cdot \eta_g \tag{8}$$

where T_{in} is the source of the torque, T_{out} is the torque amplified through the gear train, and η_g is the gear train efficiency [27].

3.1.4 Total Force Exerted on the User. In a coupled state, the user must overcome all three sources of resistance described in Secs. 3.1.1–3.1.3. The force the electrical system applies to the user, F_e, can be found using Eqs. (3) and (8)

$$F_e = \frac{T_{\text{gen}} \cdot N}{\eta_g \cdot r_c} \tag{9}$$

The force is amplified by both overall gear ratio N and r_c, the radius of the input cable's insertion point on the input pulley.

The force that inertia exerts on the user F_i can be found using Eqs. (4) and (5)

$$F_i = \frac{I_{a,i} \cdot \alpha_i}{r_c} \tag{10}$$

where α_i is the angular acceleration at the input shaft recorded by the encoder.

The force contributions from bearing friction is calculated using Eq. (7)

$$F_b = \frac{T_{b\_r}}{r_c} + \frac{N}{\eta_g \cdot r_c}\left(T_{b\_\text{gen}} + \frac{T_{b\_l}}{N \cdot \eta_g}\right) \tag{11}$$

where T_{b_r} is the first stage input shaft's deep groove ball bearing's frictional moment found using Eq. (7). T_{b_gen} is the second stage generator's deep groove ball bearing's frictional moment amplified through the gear train and subject to the gear train efficiency. T_{b_l} is the third stage frictional moment of the one-way clutch's needle roller bearings, reduced through the second stage of the gear train and subject to the gear train's inefficiencies. Finally, the spring force of the retraction mechanism F_s is calculated

$$F_s = \frac{F_{\text{const}} \cdot r_s}{r_c} \tag{12}$$

where F_{const} is the spring force provided by the manufacturer and r_s is the spring insertion radius.

The total force exerted on the user when the harvester is coupled, F, is the sum of the four force contributions mentioned above

$$F = F_e + F_i + F_b + F_s \tag{13}$$

3.2 Decoupled State ($t_c < t < t_1$). For a decoupled state, electrical power and resistance on the user become two independent solutions. Generator output is dependent on a predicted decoupled angular velocity. User resistance due to passive mechanical elements is dependent on the kinematic profile measured form the encoder.

3.2.1 Kinematic Prediction. The predicted decoupled angular velocity is found from system kinetic analysis. First, the angular acceleration of the generator shaft, α_g, is found. Conducting a decoupled moment balance at the generator shaft results in the following equation:

$$\sum M_g = T_{\text{gen}} + T_{b\_\text{gen}} + \frac{2}{N \cdot \eta_g} \cdot T_{b\_n} = I_{a,g} \cdot \alpha_g \tag{14}$$

where T_{gen} is the generator's reaction torque, T_{b_gen} is the frictional torque of the generator's bearings, and T_{b_n} is the frictional torque of the needle bearings of both drive gears, reduced by the gear ratio and subject to the gear train's efficiency. All of these are dissipative forces that equate to the product of the apparent moment of inertia, $I_{a,g}$, seen at the generator shaft and the angular acceleration of the generator shaft, α_g. From Eq. (14), the angular acceleration at the generator shaft, α_g, can be found. During system deceleration, this term will be negative indicating a net dissipative force.

Using the angular acceleration and angular velocity of the current time instant, $\omega_g(i)$, an angular velocity at the next time instant, $\omega_p = \omega_g(i+1)$, can be predicted

$$\omega_g(i+1) = \omega_g(i) + \alpha_g \cdot \Delta t \tag{15}$$

where Δt is the sampling period. The model compares ω_p, reduced through the gear train of total gear ratio N, with the angular velocity of the input shaft's encoder at the next time instant. A larger predicted angular velocity indicates decoupling (Fig. 4).

In the decoupled state, the predicted angular velocity is used to calculate electrical power produced from the generator at the next time instant, using Eqs. (1) and (2). Additionally, it is used to then further predict the angular velocity of the successive time instant using Eqs. (14) and (15).

3.2.2 Total Force Exerted on the User. When decoupled, the user interacts solely with passive mechanical elements of the harvester: the input shaft, pulley, and retraction mechanism. The force applied to the user through the input cable is the sum of the inertial loading, the retraction spring, and the bearing frictional forces. The force inertial effects exert, F_i, can be calculated using Eq. (4)

$$F_i = \frac{I_{a,d} \cdot \alpha_i}{r_c} \tag{16}$$

The apparent inertia, $I_{a,d}$, at the input shaft is the sum of the moment's of inertia of the input shaft and input pulley. The bearing frictional force, F_b, is calculated using Eq. (7)

$$F_b = \frac{T_{b\_r}}{r_c} \tag{17}$$

where T_{b_r} is the input shaft's deep groove ball bearing's frictional moment found using Eq. (7). Finally, the spring force F_s is calculated as shown in Eq. (12).

The sum of which comprises the force exerted on the user, F, through cable tension

$$F = F_i + F_b + F_s \tag{18}$$

3.3 Human Experimentation Procedure and Model Validation. A walking experiment was conducted to determine the performance of the harvester, under varying experimental configurations, and verify the model's ability to predict the voltage, electrical power, input force, and mechanical power when varying four controllable parameters: the EMF constant, armature resistance, apparent inertia, and electrical load. The experiment involved a single healthy male subject (age = 24 yrs, weight = 76 kg, and height = 181 cm) walking on a treadmill at 1.5 m/s with the harvester for 2 min. Treadmill walking was chosen for tethering off-board electronics and its ability to replicate overground walking kinematics [32,33]. A single subject was chosen to validate the proposed model, as the scope of this study was to address model accuracy. For investigation of subject variability, consult Ref. [20]. The subject reported no known gait disabilities or recent injuries. Ethical approval for the experiment was obtained from the Queen's University General Research Ethics Board.

Four different AC Maxon motors (M1–M4) and three different electrical resistance loads (3.5 Ω, 7 Ω, and 12 Ω) were used for a total of 12 testing conditions. The four motor parameters used are listed in Table 1.

All measurements were recorded using a data acquisition card (DAQ) sampling at a rate of 1000 Hz (NI PCIe6353, National Instruments, Austin, TX) through MATLAB Real Time Windows Target (Mathworks, Inc., Natick, MA). The force was measured using a load cell (Nano 25, ATI Industrial Automation, Apex, NC) in series with the input cable prefiltered using a passive second-order RC analog low-pass filter with 159 Hz cutoff frequency. Cable displacement was measured using a rotary optical encoder on the input shaft (E2, US Digital, Vancouver, WA). Voltage was measured over an electrical load using a voltage divider to scale the output voltage to be within the DAQ input range (0–5 V). High-impedance resistors were used for this application to limit the amount of current that passes through the voltage divider, which was assumed to be negligible. Current was measured over a 1 Ω high-power resistor in series with the electrical load resistance, which when combined form the total electrical load resistance for useful power generation.

The model was programmed in MATLAB. Angular displacement was first filtered with a second-order Butterworth filter of cutoff frequency 35 Hz. Cable angular velocity and acceleration were found by numerical differentiation using MATLAB's difference function (Mathworks, Inc., Natick, MA). Two performance measures, harvester output voltage and force applied to the user by the harvester, were compared to model predicted values. These two parameters were chosen as they were measured directly during data acquisition and are of importance for determining electrical output and the user input. Values were compared over ten consecutive gait cycles starting from time 1–1.5 min: a time in which the subject reached a steady state of walking. Peak values of voltage and force were compared between measured and predicted. The percent difference, $\%_{\text{error}}$, between peak model and measured voltage was calculated. Additionally, instantaneous predicted voltage and force were compared to measured values. The instantaneous error was then averaged over each step to find the instantaneous percent difference. A step was defined as heel strike of the left

Table 1 Motor specifications for all four motors. The torque constant (K_t) for each motor is equal to the EMF constant. All motors are from Maxon Motor (Switzerland).

Motor	EMF const. (mV/rad s^{-1})	Arm. res. (Ω)	M. iner. (g cm^2)
(M1) EC-i 70 W	31.52	0.807	24.2
(M2) EC 45 70 W	36.87	0.608	181
(M3) EC 45 50 W	25.13	0.464	135
(M4) EC-4 200 W	27.60	0.386	33.3

lower limb to heel strike of the right lower limb. Symmetry between both limbs was assumed, and input from the right leg only was considered. Heel strike was determined to occur, using motion capture data from Ref. [20], when cable lengthening at the end of an input cycle ceased.

Electrical power was calculated as the product of voltage and current read over the external load. Mechanical power was calculated as the product of measured cable force and velocity. Average mechanical and electrical power were found over each step to find a mean power for each testing condition. The harvester efficiency was calculated as the ratio between the measured mean electrical power and the mechanical power exerted by the user

$$\eta_{\text{tot}} = \frac{P_e}{P_m} \tag{19}$$

4 Results

The amount of electrical power generated over the 12 conditions ranged from 3.6 ± 0.1 to 15.5 ± 0.5 W (Fig. 5). Input mechanical power required to drive the device ranged from 6.9 ± 0.2 to 22.1 ± 0.6 W (Fig. 5). Overall device efficiency, found as the ratio of electrical to mechanical power, ranged from $39.8 \pm 3.2\%$ to $72.5 \pm 7.7\%$ (Fig. 5). M2 produced the most power, as expected, as a result of having the highest EMF constant (Table 1). The most efficient device configuration was M4 at the lowest resistance condition, 3.5 Ω (Fig. 5). M2 was observed to be more efficient at higher electrical resistances. M2 does require the user to input substantially more mechanical power as compared to M4, but produces more electricity.

The model was able to predict both voltage and force of the harvester given an input cable kinematic profile (Fig. 6). Peak voltage (Fig. 6(*b*)) ranged from 11.7 to 19.1 V and was predicted within $5.7 \pm 3.3\%$ error over all resistances and motor conditions. Instantaneous error was predicted within $7.0 \pm 3.8\%$. Peak force (Fig. 6(*c*)) was found to range between 15.4 and 82.1 N, which was predicted within $9.1 \pm 7.1\%$ error. Instantaneous force was predicted within $9.9 \pm 2.6\%$ error.

Using the proposed model, we can additionally explore the load applied to the user by breaking it down into individual force contributions including force for power generation, force for driving device inertia, and friction force (Figs. 7(*a*) and 7(*b*)). Electrical force is the velocity-dependent reactionary force of the generator due to electrical generation (Eq. (9)). Inertial force is the acceleration-dependent inertial force of the system (Eq. (10)). Mechanical force is the velocity- and acceleration-dependent friction force and the force of the retraction spring (Eqs. (11) and (12)). At the initiation of swing, the harvester first experiences peak acceleration, and then during midswing experiences peak velocity (Fig. 6(*a*)).

A double peak is observed in the force waveform: an early onset inertial-based force and delayed onset velocity-dependent electrical force. Superimposed, a double peak is observed where the ratio of each peak's magnitude is dependent on the inertial properties of the harvester system and the external electrical load. M2 has a larger electrical force contribution, as expected, from having a larger torque constant and back EMF constant (Fig. 7(*a*)). Additionally, due to the motor's largest moment of inertia (Table 1), the inertial component in the M2 condition is larger than that of the M4 condition. In the M2 condition, the larger inertial force results in an earlier onset peak force which loads the user during early to midswing. Conversely, with a smaller moment of inertia giving rise to a reduced first peak, M4 condition exhibits its peak force during mid to terminal swing. Such force decomposition shows how device parameters affect both magnitude and timing of the load applied to the user.

5 Discussion

To determine the best device configuration, optimal device parameters are chosen based on an intended design goal. Generating the most amount of electricity while requiring the least

Motor	Resistance (Ω)	Elec. Power (W)	Mech. Power (W)	η_{total} %
(M1) Maxon EC-i 70W	3.5	10.8±0.5	16.0±0.6	67.9±5.7
	7	5.6±0.2	11.7±0.2	47.6±3.6
	12	4.0±0.1	10.0±0.2	39.8±3.2
(M2) Maxon EC 45 70W	3.5	15.5±0.5	22.1±0.6	70.1±6.7
	7	12.4±0.8	20.2±0.9	61.6±5.1
	12	7.8±0.3	15.5±0.4	50.7±4.2
(M3) Maxon EC 45 50W	3.5	9.7±0.4	16.1±0.7	64.4±5.3
	7	7.8±0.6	15.0±0.9	52.0±4.3
	12	6.0±0.2	14.2±0.4	42.1±3.6
(M4) Maxon EC-4 200W	3.5	9.5±0.5	13.1±0.5	72.5±7.7
	7	5.1±0.2	8.2±0.3	62.2±4.6
	12	3.6±0.1	6.9±0.2	52.2±3.5

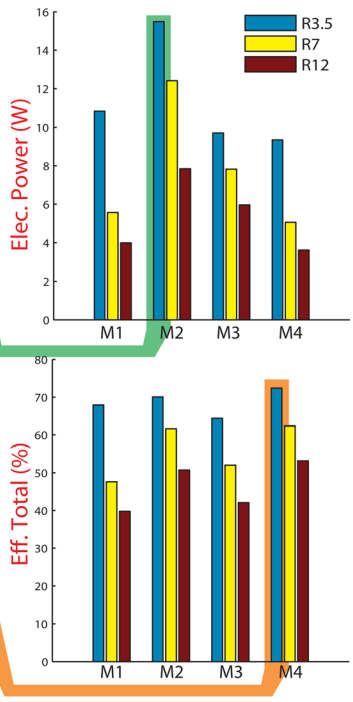

Fig. 5 Mechanical and electrical power produced in each test condition. Overall device efficiency (η_{total}) is the ratio of electrical power produced to the mechanical power required.

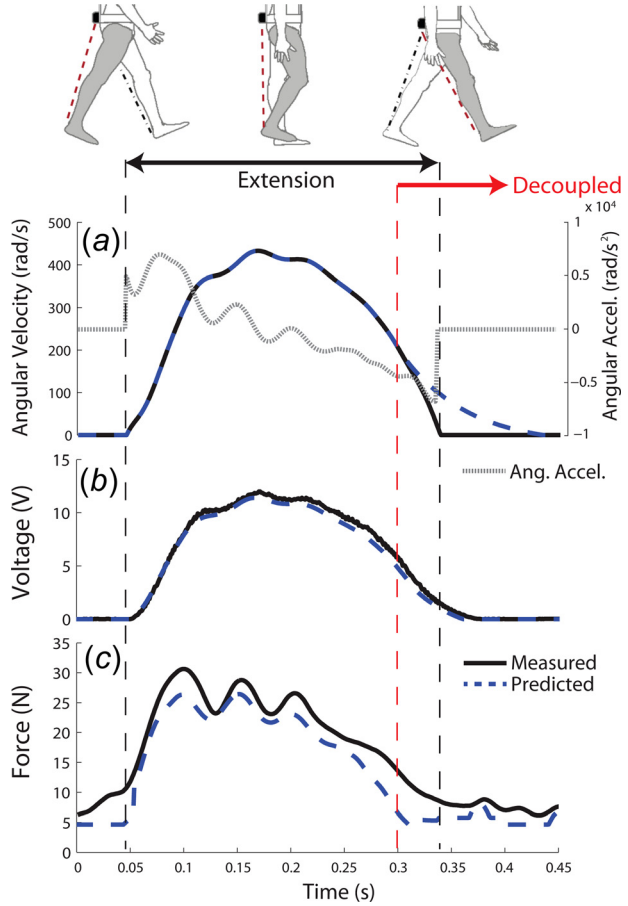

Fig. 6 (*a*) The measured input angular velocity amplified by the overall gear ratio, *N*, and the model's predicted angular velocity of the generator, showing angular velocity after decoupling. Overlaid is the measured input angular acceleration. (*b*) Measured and predicted generated voltage for the M1(R3.5) condition. (*c*) Measured and predicted force exerted on the user for the M1(R3.5) condition. The coinciding phase of gait is shown as reference. Decoupling is indicated as a vertical hatched line.

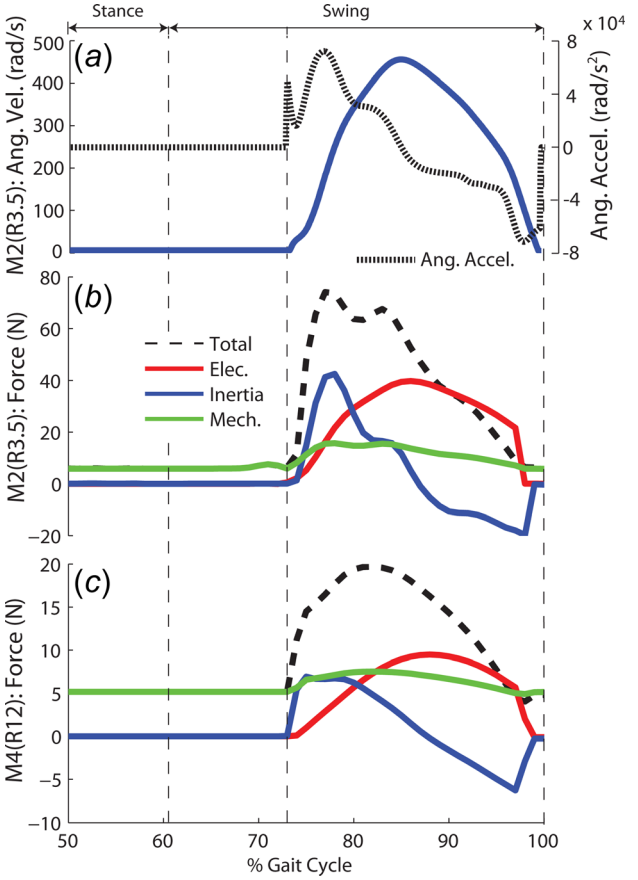

Fig. 7 (*a*) The angular velocity and angular acceleration of the M2(R3.5) condition. (*b*) and (*c*) show the electrical, inertial, and mechanical force contributions to total force, for conditions M2(R3.5) and M4(R12), respectively. Data are segmented to show a single step (50–100% of gait cycle), with vertical hatched lines indicating swing, beginning of cable extension, and the end of swing for the right leg.

amount of user effort allows for bounds to be placed on either the amount of effort required by the user or by achieving a target amount of electrical power. The most efficient condition, such as M4 at 3.5 Ω for the lower limb-driven harvester, could be chosen to maximize electricity generation while requiring the least amount of mechanical power input. Although a certain combination of the harvester parameters could be the most efficient at generating electricity, the total required mechanical power input might exceed a threshold in which it begins to affect gait kinematics. This behavior is observed in Ref. [20], where alterations in gait were observed in higher electrical load conditions. Therefore, this dynamic model can serve as a design tool for determining an appropriate range of parameter values before building a prototype. The model can be used as a tool to not only adjust the magnitude of the resistance on the user but also the timing. For the case of the lower limb-driven harvester, larger system inertia will load the user primarily during early to midswing. Conversely, altering electrical resistance affects the load on the user in mid to terminal swing. Overall resistance can therefore be tailored to better match negative power regions of the knee to efficiently harvest the most amount of energy from the user without substantially burdening them. With proper load timing and magnitude, the harvester aids in slowing down the shank during terminal swing when knee flexors are performing primarily negative work. This methodology can be applied to other harvesting methods, where we first isolate biomechanical energy available and then model and design a device that effectively targets the available energy.

For device parameters and their relationship to overall device efficiency, we notice a trend where the lowest electrical resistance (3.5 Ω) results in the highest overall efficiency for each motor tested. This is because the mechanical losses remain relatively unchanged between each testing condition. For low electrical resistance conditions, there is more electrical power being generated. Therefore, a higher portion of the input mechanical power went toward useful energy conversion rather than dissipation in heat through electrical and mechanical losses. However, with decreased electrical resistance, the internal armature resistance forms a larger portion of total resistance, therefore decreasing the electrical efficiency (Eq. (2)). Therefore, a motor with a high EMF constant ($\mathrm{mV/rad\,s^{-1}}$), low armature resistance, and low weight are all desirable features when considering generator selection. A high EMF constant would allow for more electricity generation without a high gear ratio, and therefore a possibly inefficient multiple stage gear train. Decreasing the armature resistance increases the electrical efficiency. Finally, having a low motor weight decreases the device total weight, and therefore the carrying cost of walking with the device.

From Figs. 7(*b*) and 7(*c*), it can be seen that if only the electrical force was considered, such as in the model proposed by Li et al. [6], the actual force experienced by the user would of been greatly underpredicted (22.7% peak error). This is particularly

apparent in conditions with higher system inertia such as M2 (Fig. 7(*a*)), where a larger portion of the total force is a result of inertial forces. We also understand the limitation of investigating a single walking speed during validation trials, how it may affect model performance, and ultimately the load exerted on the user. Future investigations will include multiple walking speed conditions.

The proposed dynamic model was able to accurately predict harvester output within a reasonable amount of error. Percent error for both instantaneous voltages was higher than that of peak voltage (Fig. 6(*b*)). Peak and instantaneous force error were found to be similar in value (Fig. 6(*c*)). However, high instantaneous error considered over an entire gait cycle indicates regions of less accurate force prediction. In Fig. 6(*c*), it can be seen that the two regions, the beginning and end, are typically regions with the highest prediction error. At the beginning of each input cycle, a small increase in cable tension is measured without any movement detected by the encoder, indicating a mechanical delay. Without registering cable motion, the model does not predict any increase in cable force past that of the retraction spring. This behavior highlights the model's inability to predict small fluctuations in cable tension without registered movement. Additionally, near the end of an input cycle, the model typically underpredicts the force present. This is a region of cable deceleration near decoupling. It is worth noting the negative mechanical force contribution at the end of the input cycle. This is a result of the device's components decelerating, exerting an inertial force counteracting the force required to drive the generator. At higher electrical resistances and high system inertia, this can lead to the generator acting like a flywheel, storing kinetic energy in the system for later dissipation. This results in a more continuous energy generation where in some conditions the generator never ceases to rotate during normal walking.

Predicting kinematics of the generator shaft after decoupling could be bypassed by measuring the angular velocity of the generator shaft using the hall sensor. Angular velocity of the input shaft was chosen as the input to the model because it, unlike the angular velocity at the generator shaft, is independent of harvester parameters. Generator shaft angular velocity after decoupling will change based on external electrical load and the system's moment of inertia. Therefore, if a multivariate optimization was run to find device parameters that maximize overall efficiency, a solution state where the generator runs continuously like a flywheel could exist as the generator shaft velocity is a dependent variable instead of an input variable.

6 Conclusion

This paper presented the detailed design and dynamic model of the lower limb-driven energy harvester. Model performance was validated using human walking trials in which the user walked with the lower limb-driven energy harvester in 12 testing conditions. During human experimentation, the device generated between 3.6 ± 0.1 and 15.5 ± 0.5 W of electricity with an efficiency between $39.8 \pm 3.2\%$ and $72.5 \pm 7.7\%$. The proposed energy harvesting dynamic model predicted output electrical power and input mechanical power accurately from a given input motion profile. The voltage developed was predicted with $5.6 \pm 3.2\%$ error and force exerted on the user $9.1 \pm 3.4\%$ error.

Using the proposed dynamic model, multivariate optimization could be used to find the best combination of parameters that yield a more efficient device, or perhaps optimize the device to give a desired peak user resistance. The model also provides a visual representation of both timing and magnitude of the force exerted on the user. This provides the harvester designer with more degrees-of-freedom to customize the force profile exerted on the user. These results can be used during initial design steps, or for future device iterations for energy harvesters with similar mechanical design. The model also provides a foundation toward adaptive control by providing a correlation between electrical resistance and force exerted on the user. Adaptive control can then provide the ability to optimally load a user during specific periods of gait, or adapting to gait asymmetries or deficits. Combined with human experimentation, biomechanical energy harvesting devices can be designed such that the mechanical input best matches the available biomechanical energy the harvester is targeting.

Acknowledgment

This work was supported by NSERC Discovery Grant to Q.L.

Nomenclature

BMEH = biomechanical energy harvester
DAQ = data acquisition card
EMF = electromotive force

References

[1] Romero, E., Warrington, R., and Neuman, M., 2009, "Energy Scavenging Sources for Biomedical Sensors," Physiol. Meas., **30**(9), pp. R35–62.
[2] Riemer, R., and Shapiro, A., 2011, "Biomechanical Energy Harvesting From Human Motion: Theory, State of the Art, Design Guidelines, and Future Directions," J. Neuroeng. Rehabil., **8**(1), pp. 22–35.
[3] Schertzer, E., and Riemer, R., 2015, "Harvesting Biomechanical Energy or Carrying Batteries? An Evaluation Method Based on a Comparison of Metabolic Power," J. Neuroeng. Rehabil., **12**(1), pp. 30–42.
[4] Niu, P., Chapman, P., Riemer, R., and Zhang, X., 2004, "Evaluation of Motions and Actuation Methods for Biomechanical Energy Harvesting," IEEE 35th Annual Power Electronics Specialists Conference (PESC 04), Aachen, Germany, June 20–25, Vol. 3, pp. 2100–2106.
[5] Starner, T., and Paradiso, J. A., 2004, "Human-Generated Power for Mobile Electronics," *Low-Power Electronics Design*, C. Piguet, ed., CRC Press, Boca Raton, FL, Chap. 45.
[6] Li, Q., Naing, V., Hoffer, J. A., Weber, D. J., Kuo, A. D., and Donelan, J. M., 2008, "Biomechanical Energy Harvesting: Apparatus and Method," IEEE International Conference on Robotics and Automation (ICRA), Pasadena, CA, May 19–23, pp. 3672–3677.
[7] Xie, L., and Du, R., 2012, "Harvest Human Kinetic Energy to Power Portable Electronics," J. Mech. Sci. Technol., **26**(7), pp. 2005–2008.
[8] Rome, L. C., Flynn, L., Goldman, E. M., and Yoo, T. D., 2005, "Generating Electricity While Walking With Loads," Science, **309**(5741), pp. 1725–1728.
[9] Niu, P., Chapman, P., DiBerardino, L., and Hsiao-Wecksler, E., 2008, "Design and Optimization of a Biomechanical Energy Harvesting Device," Power Electronics Specialists Conference (PESC 2008), Rhodes, Greece, June 15–19, pp. 4062–4069.
[10] Von Buren, T., Mitcheson, P. D., Green, T. C., Yeatman, E. M., Holmes, A. S., and Troster, G., 2006, "Optimization of Inertial Micropower Generators for Human Walking Motion," IEEE Sens. J., **6**(1), pp. 28–38.
[11] Romero, E., Warrington, R. O., and Neuman, M. R., 2009, "Body Motion for Powering Biomedical Devices," Annual International Conference of the IEEE Engineering in Medicine and Biology Society (EMBC 2009), Minneapolis, MN, Sept. 3–6, pp. 2752–2755.
[12] Granstrom, J., Feenstra, J., Sodano, H. A., and Farinholt, K., 2007, "Energy Harvesting From a Backpack Instrumented With Piezoelectric Shoulder Straps," Smart Mater. Struct., **16**(5), pp. 1810–1821.
[13] Xie, L., and Cai, M., 2015, "Development of a Suspended Backpack for Harvesting Biomechanical Energy," ASME J. Mech. Des., **137**(5), p. 054503.
[14] Hayashida, J. Y., 2000, "Unobtrusive Integration of Magnetic Generator Systems Into Common Footwear," Ph.D. thesis, Media Laboratory, Massachusetts Institute of Technology, Cambridge, MA.
[15] Kornbluh, R. D., Pelrine, R., Pei, Q., Heydt, R., Stanford, S., Oh, S., and Eckerle, J., 2002, "Electroelastomers: Applications of Dielectric Elastomer Transducers for Actuation, Generation, and Smart Structures," Proc. SPIE, **4698**, pp. 254–270.
[16] Gilbert, J. M., and Balouchi, F., 2014, "Design and Optimisation of a Footfall Energy Harvesting System," J. Intell. Mater. Syst. Struct., **25**(14), pp. 1746–1756.
[17] Xie, L., and Cai, M., 2015, "An In-Shoe Harvester With Motion Magnification for Scavenging Energy From Human Foot Strike," IEEE/ASME Mechatronics, **20**(6), pp. 3264–3268.
[18] Dai, D., and Liu, J., 2014, "Hip-Mounted Electromagnetic Generator to Harvest Energy From Human Motion," Front. Energy, **8**(2), pp. 173–181.
[19] Li, Q., Naing, V., and Donelan, J. M., 2009, "Development of a Biomechanical Energy Harvester," J. Neuroeng. Rehabil., **6**(1), pp. 22–34.
[20] Shepertycky, M., and Li, Q., 2015, "Generating Electricity During Walking With a Lower Limb-Driven Energy Harvester: Targeting a Minimum User Effort," PLoS One, **10**(6), p. e0127635.
[21] Rubinshtein, Z., Riemer, R., and Ben-Yaakov, S., 2012, "Modeling and Analysis of Brushless Generator Based Biomechanical Energy Harvesting System," IEEE Energy Conversion Congress and Exposition (ECCE), Raleigh, NC, Sept. 15–20, pp. 2784–2789.

[22] Pozzi, M., Aung, M. S., Zhu, M., Jones, R. K., and Goulermas, J. Y., 2012, "The Pizzicato Knee-Joint Energy Harvester: Characterization With Biomechanical Data and the Effect of Backpack Load," Smart Mater. Struct., **21**(7), p. 075023.
[23] Donelan, J., Li, Q., Naing, V., Hoffer, J., Weber, D., and Kuo, A., 2008, "Biomechanical Energy Harvesting: Generating Electricity During Walking With Minimal User Effort," Science, **319**(5864), pp. 807–810.
[24] Dell, 2016, "Inspiron 1525/1526 Product Information," Dell, Round Rock, TX, http://support.dell.com/support/edocs/systems/ins1525/en/index.htm
[25] Nokia, 2008, "Nokia 6301 Data Sheet," Nokia, Espoo, Finland.
[26] Ossur, 2009, "Proprio Foot Technical Manual," Ossur, Reykjavík, Iceland, http://assets.ossur.com/lisalib/getfile.aspx?itemid=12360
[27] Shepertycky, M., 2013, "The Development and Performance Evaluation of an Energy Harvesting Backpack," M.S. thesis, Queen's University, Kingston, ON, Canada.
[28] Maxon Motors, 2016, "Maxon DC and EC Motors," Maxon Motors, Brünigstrasse, Switzerland, accessed June 5, 2014, www.maxonmotor.com
[29] SKF, 2014, "The SKF Model for Calculating the Frictional Moment," SKF, Göteborg, Sweden.
[30] SKF, 2010, "Needle Roller Bearings," SKF, Göteborg, Sweden.
[31] Shigley, J. E., 2011, *Shigley's Mechanical Engineering Design*, Tata McGraw-Hill Education, New York.
[32] Lee, S. J., and Hidler, J., 2008, "Biomechanics of Overground vs. Treadmill Walking in Healthy Individuals," J. Appl. Physiol., **104**(3), pp. 747–755.
[33] Riley, P. O., Paolini, G., Della Croce, U., Paylo, K. W., and Kerrigan, D. C., 2007, "A Kinematic and Kinetic Comparison of Overground and Treadmill Walking in Healthy Subjects," Gait Posture, **26**(1), pp. 17–24.